

should be easily attainable under reasonable circumstances. The work shows that as laboratory conditions approach the ideal limit, the landscape is devoid of false traps in seeking to make a transition  $|i\rangle \rightarrow |f\rangle$ .

The establishment of the main results in this paper arose from separating the very complicated functional dependence of  $P_{i \rightarrow f}[C(t)]$  upon  $C(t)$  into a two-step analysis of (i)  $A_{pq}[C(t)]$  and (ii)  $\partial \langle i | \exp(iA) | f \rangle / \partial A_{pq}$ . Step (i) still involved an equally complex functional mapping of the control field in  $A[C(t)]$ ; this difficult aspect of quantum control to unravel, which is application-specific, was put aside by just drawing on the uniqueness of each functional mapping  $A_{pq}[C(t)]$  for all  $p$  and  $q$ . In this fashion, the analysis reduced to examining step (ii) through the kinematical structure in Eq. 3, which was thoroughly decomposed (23).

Our findings sharply contradict the intuitive expectation that the typically high-dimensional quantum control search spaces would generally contain suboptimal solutions. A further surprising result is the generic nature of the landscape topology deduced by the kinematic analysis. When seeking to maximize the transition  $|i\rangle \rightarrow |f\rangle$  for a controllable system of dimension  $N$ , the landscape structure is invariant to the choice of  $|i\rangle$  and  $|f\rangle$  as well as any details of the Hamiltonian. Differences in search behavior over the landscape can in practice arise due to the particular nature of the Hamiltonian and the control. Nevertheless, the optimal control landscape topology identified in this work is universal.

#### References and Notes

- H. Rabitz, R. de Vivie-Riedle, M. Motzkus, K. Kompa, *Science* **288**, 824 (2000).
- S. A. Rice, M. Zhao, *Optical Control of Molecular Dynamics* (Wiley, New York, 2000).
- R. S. Judson, H. Rabitz *Phys. Rev. Lett.* **68**, 1500 (1992).
- C. J. Bardeen et al., *Chem. Phys. Lett.* **280**, 151 (1997).
- R. J. Levis, G. M. Menkir, H. Rabitz, *Science* **292**, 709 (2001).
- A. Assion et al., *Science* **282**, 919 (1998).
- D. Meshulach, Y. Silberberg, *Nature* **396**, 239 (1998).
- T. Weinacht et al., *Chem. Phys. Lett.* **344**, 333 (2001).
- R. Bartels et al., *Nature* **406**, 164 (2000).
- J. Kunde et al., *J. Opt. Soc. Am. B* **18**, 872 (2001).
- T. Hornung et al., *Appl. Phys. B Lasers Opt.* **71**, 277 (2000).
- C. Daniel et al., *Chem. Phys.* **267**, 247 (2001).
- J. L. Herek et al., *Nature* **414**, 57 (2001).
- T. Brixner et al., *J. Mod. Opt.* **50**, 539 (2003).
- W. Zhu, H. Rabitz, *Int. J. Quant. Chem.* **93**, 50 (2003).
- D. Zeidler, S. Frey, K. L. Kompa, M. Motzkus, *Phys. Rev. A* **64**, 023420 (2001).
- B. J. Pearson, J. L. White, T. C. Weinacht, P. H. Bucksbaum, *Phys. Rev. A* **63**, 063412 (2001).
- M. Demiralp, H. Rabitz, *Phys. Rev. A* **47**, 809 (1993).
- V. Ramakrishna, M. V. Salapaka, M. Dahleh, H. Rabitz, A. Peirce, *Phys. Rev. A* **51**, 960 (1995).
- G. Turinici, H. Rabitz, *J. Phys. A Math. Gen.* **36**, 2565 (2003).
- M. D. Girardeau, S. G. Schirmer, J. V. Leahy, R. M. Koch, *Phys. Rev. A* **58**, 2684 (1998).
- The replacement of Eq. 3 over Eq. 2 for optimality analysis requires the criteria that the set of functions  $\{(\delta A_{pq})/(\delta C(t))\}$  be linearly independent. The analysis in this paper assumes that the entire  $N$ -dimensional quantum system is controllable. In particular, the  $N$  states could be the controllable portion of a larger system whose other states are not addressed by the control.
- Supporting analysis is available on Science Online.
- H. Rabitz, M. Hsieh, C. Rosenthal, unpublished results.
- J. M. Geremia, W. Zhu, H. Rabitz, *J. Chem. Phys.* **113**, 10841 (2000).
- A. M. Weiner, *Rev. Sci. Instrum.* **71**, 1929 (2000).
- R. Wu, I. Sola, H. Rabitz, unpublished results.
- The authors acknowledge NSF and ARO-MURI.

#### Supporting Online Material

www.sciencemag.org/cgi/content/full/303/5666/1998/DC1  
SOM Text

13 November 2003; accepted 12 February 2004

## Atomic-Resolution Measurement of Oxygen Concentration in Oxide Materials

C. L. Jia and K. Urban\*

Using high-resolution imaging at negative spherical aberration of the objective lens in an aberration-corrected transmission electron microscope, we measure the concentration of oxygen in  $\Sigma 3\{111\}$  twin boundaries in  $\text{BaTiO}_3$  thin films at atomic resolution. On average, 68% of the boundary oxygen sites are occupied, and the others are left vacant. The modified  $\text{Ti}_2\text{O}_9$  group unit thus formed reduces the grain boundary energy and provides a way of accommodating oxygen vacancies occurring in oxygen-deficient material by the formation of a nanotwin lamellae structure. The atomically resolved measurement technique offers the potential for studies on oxide materials in which the electronic properties sensitively depend on the local oxygen content.

Oxygen features eminently in materials that are of considerable technical importance. Such materials include the large group of electroceramic materials comprising dielectrics, ferroelectrics, piezoelectric materials, and ionic conductors (1). An example is  $\text{BaTiO}_3$ , which is used in multilayer ceramic capacitors and in positive-temperature coefficient thermistors (2). Because of their high permittivity, thin films of barium-based perovskites, e.g.,  $(\text{Ba}_x\text{Sr}_{1-x})\text{TiO}_3$ , are being intensively studied as dielectrics in future generations of semiconductor-based dynamic random access memories. Recently, the perovskite-type high-temperature superconductors (3) and the colossal magnetoresistance materials (4) have attracted considerable attention. In all these materials, the physical properties are sensitively controlled by the oxygen stoichiometry. In extended crystal defects, e.g., grain boundaries and dislocations, the oxygen occupancy of lattice sites can deviate substantially from the stoichiometric value either because of structural constraints or as a result of the interaction of charged mobile oxygen vacancies with the electrically active defects (1, 5–8). Indeed, the success of oxide materials for electronic applications depends crucially on the solutions found to overcome lattice defect-related problems. As a starting point, it is necessary

to understand the structure of defects and how their electronic properties are influenced by deviations of the local oxygen concentration from stoichiometry. A key issue in this endeavor is to be able to measure the oxygen occupancy of lattice sites in or close to defects. Such measurements will allow us to construct the realistic structural models required to carry out quantum-mechanical calculations and to eventually control the electronic properties of real oxide materials.

Unfortunately, the structural techniques available for studying oxygen in oxides, x-ray and neutron scattering, as well as in electron crystallography, yield the spatially averaged structure and do not allow defects to be studied. Of the microscopic techniques, the contrast based on the high-angle scattering of electrons (Z-contrast) in scanning transmission electron microscopy does not allow oxygen to be imaged because it is confined to elements with a high value of the nuclear charge  $Z$  (9). In addition, it is not yet feasible to measure the local oxygen occupancy by conventional high-resolution transmission electron microscopy (HRTEM), owing to a lack of resolution and contrast. Nor has a technique been developed to derive an oxygen occupancy from a local image intensity in HRTEM (10–13). Information on oxygen in defects has been derived from electron-energy loss spectroscopy (EELS) carried out with an electron microscope. However, this technique does not allow the oxygen occupancy to be measured either. Because of limited instrumental resolution and signal-to-noise ratio, the oxygen signal arises from a relatively

Institute for Solid State Research, Research Center Jülich, D-52425 Jülich, Germany.

\*To whom correspondence should be addressed. E-mail: k.urban@fz-juelich.de

large area, including both the defect and the matrix, with the result that a mixture of bulk- and defect-specific spectra is recorded. Nevertheless, results obtained for a  $\Sigma 3\{111\}$  twin boundary in  $\text{BaTiO}_3$  (14), an  $8^\circ$   $[001]$  tilt grain boundary (9), and a  $[100]$  dislocation (15) in  $\text{SrTiO}_3$  were qualitatively interpreted in terms of an oxygen deficiency of the defect structure.

By imaging at a negative value of the spherical aberration coefficient,  $C_s$ , of the objective lens of a transmission electron microscope equipped with a spherical-aberration corrector, elements with low nuclear charge can be imaged at atomic resolution even in instances where the atoms are situated a short distance away from strongly scattering heavy atoms (16). By this method, oxygen can be imaged at proven atomic resolution in  $\text{SrTiO}_3$  and in  $\text{YBa}_2\text{Cu}_3\text{O}_7$ . The basic rationale underlying the negative  $C_s$  imaging (NCSI) technique is that linear and nonlinear contrast contributions add up constructively, yielding high-intensity maxima at atomic column positions, whereas these contributions are mutually reduced in the alternative conventional imaging modes (17).

Here, we demonstrate that the NCSI technique is suitable not only for imaging oxygen but also for performing quantitative measurements of oxygen occupancy at atomic resolution at lattice defects in oxides. For this purpose, we propose a technique that allows us to correlate the image intensity signal of an oxygen atomic column with its occupancy. This technique is applied to the  $\Sigma 3\{111\}$  grain boundary occurring in the  $\{111\}$  twin lamella structure in  $\text{BaTiO}_3$  thin films (18, 19), particularly if the films are prepared under conditions in which the material becomes oxygen deficient (20).

The  $\text{BaTiO}_3$  thin films are grown by pulsed-laser deposition at  $750^\circ\text{C}$  on the platinum layer of  $\text{Pt/Ti/SiO}_2/\text{Si}$  heterostructure wafers in an oxygen atmosphere at 0.1 mbar. Plan-view specimens for HRTEM are prepared by using standard procedures. We use the Jülich Philips CM 200 FEG microscope at an electron-accelerating voltage of 200 kV. The instrument is equipped with a spherical-aberration corrector (21) which, for the NCSI technique, is adjusted to  $C_s = -40 \mu\text{m}$ , i.e., close to the optimum phase-contrast value derived in (16, 17). Images are recorded by a charge-coupled device camera with 1024 by 1024 pixels at a sampling rate of  $\sim 0.02 \text{ nm/pixel}$  (22).

Figure 1A shows an image of a  $\text{BaTiO}_3$   $[110]$  crystal. Embedded in a "matrix" of crystal orientation "I" are nanometer-scale  $(\bar{1}\bar{1}1)$  and  $(1\bar{1}1)$  twin lamellae of orientation "II" and "III," respectively. The magnified image in Fig. 1B indicates that the oxygen-atom columns located between two Ti columns are imaged with strong contrast, both in the matrix and in the twin boundary plane (vertical black arrows).

In HRTEM, the atom columns are aligned with the electron-beam direction, and therefore the intensity signal averages over the atomic

occupation along a given column. The ultimate lateral resolution is given by the information limit of the electron microscope, defined as the

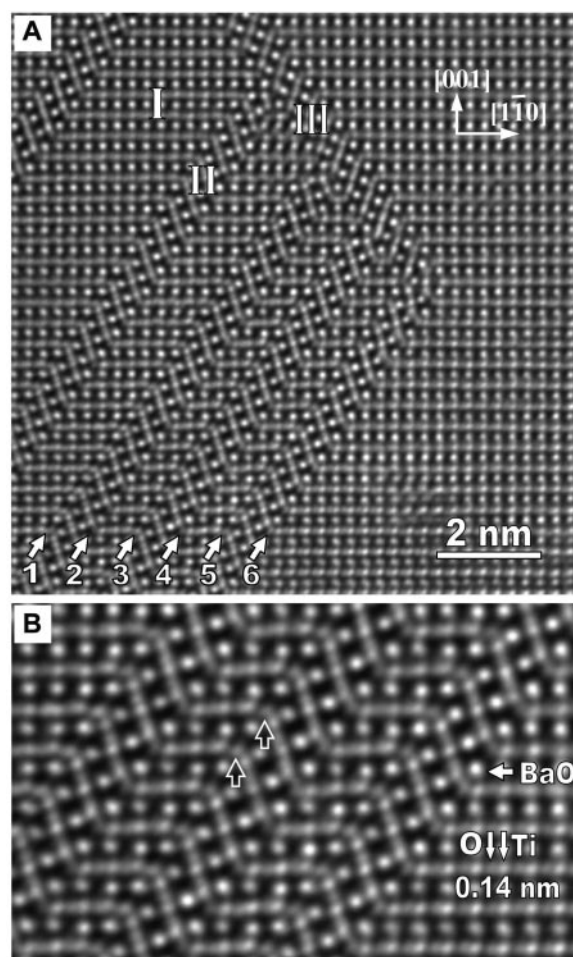


**Fig. 1.** (A) Image of the atomic structure of  $\text{BaTiO}_3$   $[011]$  obtained using the NCSI technique. Atom sites appear bright on a dark background. Lamellae of two twin variants II and III are seen in matrix I. The twin boundaries for which the oxygen-atom concentration is measured are labeled 1 to 6. (B) Magnified image of the twinned area. The two vertical dark arrows indicate, as an example, two of the oxygen-atom positions in the twin-boundary plane.

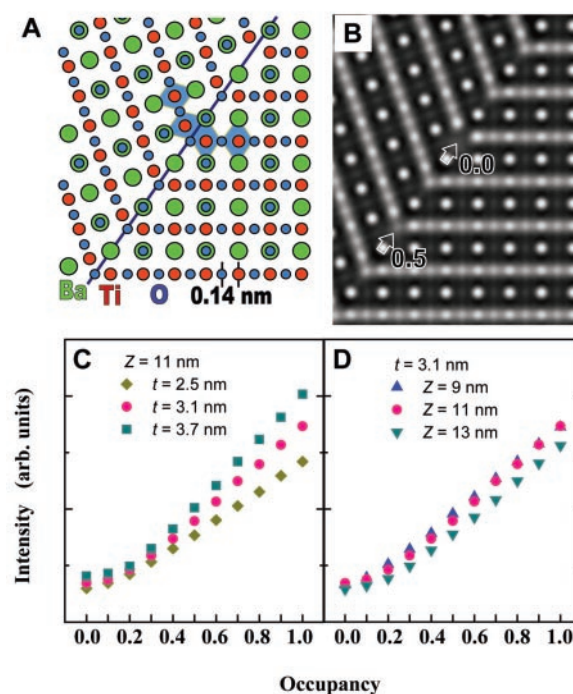


**Fig. 2.** (A) The structure of the  $\Sigma 3\{111\}$  twin boundary in  $[110]$  projection. (B) Calculated image of the boundary (spherical-aberration coefficient:  $-40 \mu\text{m}$ ; specimen thickness: 3.1 nm; defocus:  $+9 \text{ nm}$ ; semi-angle of beam convergence: 0.2 mrad; defocus spread: 5.6 nm). Two arrows mark oxygen columns with an occupancy of 0 and 0.5, respectively. (C) Plot of the image intensity of oxygen sites in the boundary plane versus occupancy calculated for thicknesses  $t = 2.5, 3.1$ , and  $3.7 \text{ nm}$  and for defocus  $Z = +11 \text{ nm}$ . (D) Plot of the intensity versus oxygen-site occupancy calculated for a thickness of 3.1 nm and for the defocus values of 9, 11, and 13 nm, respectively. For an occupancy higher than 0.3, the intensity increases linearly with occupancy.



inverse of the highest spatial frequency transmitted through the instrument contributing to the image. For our instrument, the value of the information limit is measured as  $\sim 0.125$  nm (23). The closest atomic distance occurring in the [110] projection of the  $\text{BaTiO}_3$  crystal lattice is that of the oxygen-titanium pairs 0.14 nm apart. Therefore, the resolution defined by the information limit is sufficient to image these two types of atoms separately. However, to obtain a reliable measurement of the occupancy of a given atomic column, an additional precondition has to be met: The image intensity measured at the position of a given atomic column must be free of contributions arising from electron scattering at the neighboring atomic columns. This is guaranteed only if the contrast delocalization defined by the radius of the point-spread function,  $R_s$ , which depends on spherical aberration and defocus of the objective lens (24), is sufficiently low. One advantage of the NCSI mode is that contrast delocalization is very low (16). Under the conditions used in this work,  $R_s \approx 0.08$  nm. Therefore, the image intensity at the position of an oxygen site remains essentially unaffected by scattering at the neighboring Ti sites, providing genuine atomic resolution.

A prerequisite for quantitative measurements is knowledge of how the image intensity of an individual column depends on oxygen occupancy, i.e., on the fraction of column sites (along the viewing direction) occupied by oxygen atoms. This relation can be obtained by numerical solution (25) of the Schrödinger equation for variable oxygen-column scattering potential using the multislice technique (26, 27). In this way, the

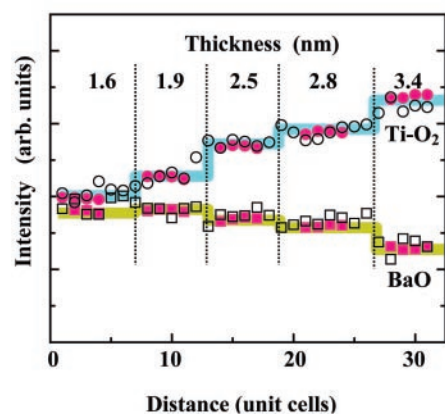


**Fig. 3.** Plot of an intensity function versus distance from top to bottom in Fig. 1A (in units of the [001] lattice parameter of 0.4 nm). The function is obtained by integrating for the matrix area on the right-hand side of Fig. 1A the intensity values along the horizontal [110] direction over a horizontal distance of  $\sim 3.5$  nm. Black open squares: BaO; black open circles:  $\text{Ti-O}_2$ . The corresponding steps in the BaO and the  $\text{Ti-O}_2$  signals indicate that the sample thickness increases in steps of two and three atomic monolayers in height. The filled squares and filled circles depict values calculated for a defocus of 9 nm and the thicknesses indicated.

image in Fig. 2B is calculated for a sample thickness of 3.1 nm using the structure model (28) shown in Fig. 2A. Two arrows in the calculated image mark oxygen columns for which the occupancy is set to 0 and 0.5. The corresponding change in contrast is restricted to the column position itself, providing evidence for actual atomic resolution. Figure 2, C and D, depict the calculated peak intensity of the oxygen columns as a function of occupancy for different sample thicknesses,  $t$ , and defocus values,  $Z$ , respectively. We find that the intensity depends both on thickness and defocus, and, for occupancy values  $>0.3$ , increases linearly with occupancy.

The use of this relation for oxygen-occupancy measurements presents at least two difficulties. First, in HRTEM, it is difficult to measure absolute intensities that could then be directly compared to calculated values. Therefore, we restrict ourselves to relative occupancy values, taking the intensity of the oxygen signal in the matrix as a reference. Second, neither the absolute value of the objective-lens defocus nor that of the sample thickness is known with sufficient accuracy. This problem is overcome by an iterative procedure, in which, for a sample area far away from the boundaries, the intensities are calculated and compared with the measured values. In particular, we exploit the substantially different thickness dependences of the signal from the Ti- and Ba-containing atom columns for an accurate determination of the imaging parameters (29–31).

The measurements are performed in three steps. For Step I, we study the matrix area on the right-hand side of Fig. 1A. By integrating the intensity values (at pixel resolution) along [110] over a distance of  $\sim 3.5$  nm, we obtain an intensity function (32) whose maxima are plotted (open symbols) in Fig. 3 versus distance from the top of Fig. 1A (in units of the [001] lattice parameter of 0.4 nm). We note that the intensity-labeled “ $\text{Ti-O}_2$ ” in Fig. 3 arises from both the Ti and the  $\text{O}_2$  columns. We find that the  $\text{Ti-O}_2$  signal increases whereas the BaO signal decreases with distance. In addition, we recognize cor-

responding steps in both intensity curves. The filled symbols represent calculated values obtained for  $Z = 9$  nm and the thickness values indicated. In these calculations the objective-lens defocus, the sample thickness, and the scaling factor (33–35) required for a quantitative comparison of calculated and experimental image contrast were taken as variables and optimized iteratively until an optimum and stable fit to the whole range of experimental values was achieved.

The results of Fig. 3 can be understood if we assume a wedge-shaped sample whose thickness increases roughly vertically in Fig. 1A, from top to bottom. However, the thickness does not change continuously, but rather increases in steps of 0.3 and 0.6 nm in height. These values correspond to  $2\Delta$  and  $4\Delta$ , where  $\Delta$  is the thickness of a {110} atomic monolayer of  $\text{BaTiO}_3$ . The simultaneous measurement of both the  $\text{Ti-O}_2$  and the BaO signal permits a very accurate determination of thickness and defocus because, owing to the difference in effective extinction distance, the thickness dependence of the Ti (nuclear charge 22) intensity differs substantially from that of Ba (nuclear charge 56).

In Step II, in the area of the twin lamellae (containing the twin boundaries “1” to “6”) in Fig. 1A, we measure the individual intensity profiles of all Ti, BaO, and  $\text{O}_2$  sites, with the exception of the oxygen sites in the boundary planes. From these data, we calculate an average peak value for each of these three types of sites. Repeating the iterative computer-based fit, we find that the overall fit to all our data can be improved further by the introduction of a deviation of  $0.6^\circ$  from the exact Laue orientation. In this way, a simultaneous fit to all three peak values within an error of  $\pm 2\%$  is obtained. For the lamellae area, we obtain  $Z = 9.2$  nm and  $t = 3.1$  nm as parameters that must be considered in the evaluation of the intensities measured for the oxygen sites in the boundary plane.

This quantitative basis now permits, in Step III, a determination of the occupancy of the individual oxygen sites in the boundary planes of the twins “1” to “6”. In Fig. 4, the data for boundary “4” are given as an example. The occupancy values calculated on the basis of the measured intensities range from 0.4 to 0.7. From the data obtained for all six boundaries, we derive a mean value for the occupancy of  $0.68 \pm 0.02$  at a standard deviation of 0.16. With respect to the measurement error, the scatter of the intensity values measured for the individual oxygen sites in the matrix area leads to essentially the same values for the deviation from the mean occupancy (assumed to be 1) and for the standard deviation.

The implications of our results are twofold. First, we have shown that atomic-resolution oxygen-concentration measurements can be carried out by HRTEM using the NCSI technique. By a combination of computer-based image simula-

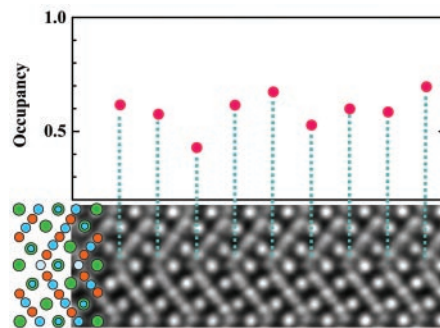


**Fig. 4.** Section of the twin boundary “4” (Fig. 1) with the grain-boundary oxygen sites indicated. The occupancy values derived from the measured intensities are shown as filled red circles.

tion and quantitative intensity measurements, the oxygen occupancy of individual lattice sites in defects can be measured. The basis for this is provided by the fact that the oxygen image signal depends linearly on occupancy and that the imaging parameters required for a quantitative evaluation can be determined by exploiting the dependence of the image signal of the neighboring cation columns on these parameters. The technique that we have described can be applied to more extensive studies on defects in oxides. In view of their importance in determining the electronic properties of these materials, quantitative oxygen concentration measurements offer potential, for example, in assessing the role of oxygen in grain-boundary Josephson junctions in oxide superconductors. Our technique is, however, not limited to oxides but can be applied to compounds such as nitrides and borides, in which deviations from stoichiometry with respect to low-nuclear charge atoms control the physical properties.

Second, our measurements provide quantitative evidence for a substantial reduction of the oxygen occupancy, i.e., the presence of oxygen vacancies in the  $\Sigma 3\{111\}$  twin boundaries in  $\text{BaTiO}_3$ . On average, 68% of the boundary oxygen sites are occupied and the others, about one site out of three, are left vacant. The error in the mean occupancy can be accounted for by an atomic-scale specimen surface roughness. Also, despite the low sensitivity of  $\text{BaTiO}_3$  to electron radiation damage, a contribution of radiation-induced chemical disorder cannot be entirely ruled out.

From the results of an EELS study of the near-edge structure of the  $L_{23}$  ionization edge of Ti in the  $\Sigma 3\{111\}$  twin boundary, it was concluded that the Ti atoms adjacent to the boundary plane occur in an oxidation state lower than the +4 on the stoichiometric compound (14). This suggests that the boundary plane is oxygen deficient. In the  $\Sigma 3\{111\}$  twin boundary, the original  $\text{TiO}_6$  octahedra change from corner- to face-sharing, forming a  $\text{Ti}_2\text{O}_9$  group unit. This group is a genuine element of the  $\text{BaTiO}_3$  system because it is also the basic structural element of the hexagonal high-temperature phase formed from the cubic phase at  $\sim 1460^\circ\text{C}$  (28, 36). In a study performed by x-ray scattering on  $\text{BaTiO}_3$  in which tetravalent  $\text{Ti}^{4+}$  was replaced by trivalent  $\text{Fe}^{3+}$ , the hexagonal phase was obtained (37). In this hexagonal  $\text{Ba}(\text{Ti}_{1-x}\text{Fe}_x)\text{O}_3$  phase, those sites [called O(1) sites] of the  $\text{Ti}_2\text{O}_9$  group unit that correspond to the oxygen sites in our  $\Sigma 3\{111\}$  twin boundary plane are left partially vacant. When the iron content of the compound is varied, there is a maximum concentration of  $\text{Fe}^{3+}$  that can be accommodated. If we assume that the corresponding oxygen vacancies are all confined to the O(1) sites, this corresponds to an occupancy in which one oxygen atom in three is missing. Because the structure of the bulk hexagonal phase and the structure of the  $\Sigma 3\{111\}$  twin boundary are both based on the  $\text{Ti}_2\text{O}_9$  group

unit, our measured oxygen occupancy of 68% for the oxygen boundary sites is in excellent agreement with the results obtained in the bulk  $\text{Ba}(\text{Ti}_{1-x}\text{Fe}_x)\text{O}_3$  phase. Thus, the incorporation of oxygen vacancies reduces the grain boundary energy and allows the system to react to oxygen-deficient conditions, e.g., during thin-film deposition, by the formation of a nanotwin lamella structure.

To date no theoretical calculations are available for an oxygen-deficient structure of the  $\Sigma 3\{111\}$  twin boundary in  $\text{BaTiO}_3$ . However, for  $\text{SrTiO}_3$ , it has recently been shown by first-principles calculations that incorporation of oxygen vacancies in the grain boundary plane is expected to reduce the total energy of the boundary even though the Ti valence deviates from the value in the stoichiometric compound (9, 38). Our measurements now open up the possibility of constructing realistic models for advanced electronic-structure calculations in these materials.

# References and Notes

1. N. Setter, R. Waser, *Acta Mater.* **48**, 151 (2000).
2. H.-I. Yoo, C.-R. Song, D.-K. Lee, *J. Electroceram.* **8**, 5 (2002).
3. C. P. Poole, H. A. Farach, R. J. Creswick, *Superconductivity* (Academic Press, San Diego, CA, 1995).
4. Y. Tokura, *Colossal Magnetoresistive Oxides* (Gordon & Breach, London, 2000).
5. R. Waser, *Integr. Ferroelect.* **15**, 39 (1997).
6. A. K. Tagantsev, I. Stolichnov, E. L. Colla, N. Setter, *J. Appl. Phys.* **90**, 1387 (2001).
7. R. Waser, *Solid State Ionics* **75**, 89 (1995).
8. R. F. Klie, Y. Ito, S. Stemmer, D. N. Browning, *Ultramicroscopy* **86**, 289 (2001).
9. M. Kim et al., *Phys. Rev. Lett.* **86**, 4056 (2001).
10. A. Ourmazd, J. C. H. Spence, *Nature* **329**, 425 (1987).
11. N. P. Huxford, D. J. Eaglesham, C. J. Humphreys, *Nature* **329**, 812 (1987).
12. G. Van Tendeloo, T. Krekels, in *Characterization of High  $T_c$  Materials & Devices by Electron Microscopy*, N. D. Browning, S. J. Pennycook, Eds. (Cambridge Univ. Press, Cambridge, 2000), pp. 161–191.
13. Z. Zhang, W. Sigle, F. Phillipp, M. Rühle, *Science* **302**, 846 (2003).
14. A. Recnik et al., *Philos. Mag. B* **70**, 1021 (1994).
15. Z. Zhang, W. Sigle, M. Rühle, *Phys. Rev. B* **66**, 94108 (2002).
16. C. L. Jia, M. Lentzen, K. Urban, *Science* **299**, 870 (2003).
17. C. L. Jia, M. Lentzen, K. Urban, *Microsc. Microanal.*, in press.
18. C. L. Jia et al., *Philos. Mag. A* **77**, 923 (1998).
19. T. Suzuki, Y. Nishi, M. J. Fujimoto, *J. Am. Ceram. Soc.* **83**, 3185 (2000).
20. K. P. Fahey, B. M. Clemens, L. A. Wills, *Appl. Phys. Lett.* **67**, 2480 (1995).
21. M. Haider et al., *Nature* **392**, 768 (1998).
22. All intensity data are taken from the original unfiltered images.
23. M. Lentzen et al., *Ultramicroscopy* **92**, 233 (2002).
24. H. Lichte, *Ultramicroscopy* **38**, 13 (1991).
25. All calculations and numerical image simulations were carried out with the *MacTempas* software package (M. A. O'Keefe, R. Kilaas; National Center for Electron Microscopy, Lawrence Berkeley National Laboratory, Univ. of California).
26. J. M. Cowley, A. F. Moodie, *Acta Crystallogr.* **10**, 609 (1957).
27. M. A. O'Keefe, R. Kilaas, *Scanning Microsc. Suppl.* **2**, 225 (1988).
28. C. L. Jia, A. Thust, *Phys. Rev. Lett.* **82**, 5052 (1999).
29. A. Ourmazd, F. H. Baumann, M. Bode, Y. Kim, *Ultramicroscopy* **34**, 237 (1990).
30. D. Stenkamp, W. Jäger, *Ultramicroscopy* **50**, 321 (1993).
31. C. Kisielowski et al., *Ultramicroscopy* **58**, 131 (1995).
32. The computer code "Digital Micrograph" (GATAN) is used for this purpose.
33. M. J. Hytch, W. M. Stobbs, *Ultramicroscopy* **53**, 63 (1994).
34. A. Thust, K. Urban, *Ultramicroscopy* **45**, 23 (1992).
35. W. E. King, G. H. Campbell, *Ultramicroscopy* **56**, 46 (1994).
36. R. D. Burbank, H. T. Evans, *Acta Crystallogr.* **1**, 330 (1948).
37. I. E. Grey et al., *J. Solid State Chem.* **135**, 312 (1998).
38. R. Astala, P. D. Bristowe, *J. Phys. Condens. Matter* **14**, 6455 (2002).
39. We thank A. Thust, M. Lentzen, K. Tillmann, and L. Houben for fruitful discussions and comments on the manuscript.

13 November 2003; accepted 13 February 2004

## Oxygen Isotope Constraints on the Sulfur Cycle over the Past 10 Million Years

Alexandra V. Turchyn\* and Daniel P. Schrag

Oxygen isotopes in marine sulfate ( $\delta^{18}\text{O}_{\text{SO}_4}$ ) measured in marine barite show variability over the past 10 million years, including a 5 per mil decrease during the Plio-Pleistocene, with near-constant values during the Miocene that are slightly enriched over the modern ocean. A numerical model suggests that sea level fluctuations during Plio-Pleistocene glacial cycles affected the sulfur cycle by reducing the area of continental shelves and increasing the oxidative weathering of pyrite. The data also require that sulfate concentrations were 10 to 20% lower in the late Miocene than today.

Sulfate plays an important role in the modern ocean, serving as the primary oxidant for much of the organic matter and nearly all of the methane produced in ocean sediments (1, 2). The biogeochemical cycle of marine sulfate has been assumed to be relatively stable,

with a long residence time of  $\sim 10^7$  years (3–6). Studies of marine sulfate, focusing largely on variations of sulfur isotopes in sedimentary pyrite (7, 8), have concluded that sulfate concentrations were low in the Archean, increased in the Proterozoic to modern